

The new face of multifractality: Multi-branchness and the phase transitions in time series of inter-event times

Jarosław Klamut* and Ryszard Kutner

Faculty of Physics, University of Warsaw, Pasteur Str. 5, PL-02093 Warsaw, Poland

Tomasz Gubiec

Center for Polymer Studies and Department of Physics,

Boston University, Boston, MA 02215 USA and

Faculty of Physics, University of Warsaw, Pasteur Str. 5, PL-02093 Warsaw, Poland

Zbigniew R. Struzik

University of Tokyo, Bunkyo-ku, Tokyo 113-8655, Japan and

Advanced Center for Computing and Communication,

RIKEN, 2-1 Hirosawa, Wako 351-0198, Saitama, Japan

We develop an extended multifractal analysis based on the Legendre-Fenchel transform (sometimes referred to as Legendre multi-branched one) rather than the routinely used canonical Legendre transform. In our variant of coarse-graining pre-processing, the local detrending of time series has been replaced by an appropriate averaging over days combined with properly-suited detrending on a daily time scale. This new approach is devoid of troublesome artifacts in the form of innumerable faults of these local trends that can deform the hierarchy of fluctuations and hence the final multifractality. Notably, our analysis is sensitive to the change of time scale as it should be. This analysis has developed, e.g., for empirical time series of inter-event or waiting times, which are an essential element of the popular continuous-time random walk formalism. The core of this extended multifractal analysis is the non-monotonic behavior of the generalized Hurst exponent – the fundamental exponent of the study – and hence a multi-branched spectrum of dimensions, which for our case is additionally of the left-sided one. We examine the main thermodynamic consequences of the existence of this type of multifractality. They can be expressed directly in the language of thermally stable, metastable, and unstable phases, and phase transitions between them as well. These phase transitions are of the first and second orders according to the modified Ehrenfest classification, sometimes called the Mandelbrot one.

PACS numbers: 89.65 Gh, 05.40.-a, 89.75.Da

I. INTRODUCTION

A. General remarks

The concept of extended scale invariance referred to as multifractality, has become a routinely applied but still intensively developed methodology for studying both complex systems [1–5, 7] and nonlinear (e.g., chaotic with a low degree of freedom) dynamical ones [8]. It is a rapidly evolving and inspiring approach to nonlinear science in many different fields stretching far beyond traditional physics [9].

The direct inspiration of the present work is our earlier results presented in papers [10, 11]. In these publications, we found the left-sided multifractality on financial markets as a direct result of a non-analytic behavior of the Rényi exponent. We indicated that a broad distribution of inter-event times is

responsible for the existence of left-sided multifractality. In the present work, we suggest that primarily nonlinear long-term autocorrelations bear responsibility for the multifractality observed.

Attention was first drawn to the existence of left-sided multifractality by Mandelbrot and coauthors [12, 13]. This multifractality was generated by the binomial cascade, which produces singularity in the Rényi exponent or stretched exponential decay of the smallest coarse-grained probability. Blumenfeld and Aharony [14] discovered an exciting breakdown of multifractality in diffusion-limited aggregation. They found strongly asymmetric spectra of singularity depending on the size of the growing aggregate in DLA, showing an apparent tilt to the left as a signature of the phase transition to non-multifractality. Earlier, the multifractals with the right part of the spectrum of singularities not well defined (caused by a phase transition), were mimicked by a random version of the paradigmatic two-scale Cantor set and also in the domain of DLA [15–18] (and refs therein).

* Jaroslaw.Klamut@fuw.edu.pl

In recent years much effort has been devoted to the reliable identification of the real multifractality in real data. These data are coming from various fields such as geophysics [19], seismology [20] and hierarchical cascades of stresses in earthquake pattern [21, 22], from the atmospheric science and climatology, e.g., turbulent phenomena [23, 24], financial markets [25, 26], neuroscience [27], e.g., neuron spiking [28], from cardio-science or cardio-physics [29], e.g., physiology of the human heart [30] and refs. therein, and from further works investigating complexity in heart rate [31, 32] and physiology [33]. However, the identification of true multifractality is still a challenge because there are many circumstances in which an apparent (spurious) multifractality appears.

The non-spurious (real) multifractality occurs where fluctuations and/or dependences arise in many different spatial and/or temporal scales under different scaling laws i.e., defined by various scaling exponents, which create a multiscaling phenomenon. For example, multifractality can be caused by the long-term dependence (e.g., temporal nonlinear long-term autocorrelations) or/and some broad distributions, leading to the hierarchical organization of many scales. The identification of multifractality in empirical data requires caution, not only due to the finite-size effect [34] and crashes [35] (i.e., strong non-stationarities) but also because of the presence of spurious [36] and/or corrupted multifractality [37]. Fortunately, because multifractality is sometimes sensitive to these effects (or contaminations), they can be appropriately identified and eliminated or at least minimized. We also deal with a situation when the role of the finite-size effect is small compared to other factors. Recognizing the non-spurious multifractality is all the more difficult because we are not sure that all sources of multifractality have discovered to date [38] and because one has to deal with physical multifractality of limited range; also, the limited amount of empirical data available is a serious technical challenge. These last two hurdles can be the sources of finite size effects, which sometimes manages to disarm by finite-size scaling.

There are also other difficulties with the identification of real multifractality, primarily when nonlinear properties of time series are studied. A spurious multifractality can also arise as a result of slow crossover phenomenon on finite time scales [39]. Besides, the pollution of a multifractal signal with noise (white or colored) as well as the presence of short memory or periodicity can significantly change the properties of the multifractal signal.

Unfortunately, the origin of multifractality is, in

fact, rarely identified. Only two sources of true multifractality have been known to date [38]: (i) presence in the system of broad distributions and/or (ii) long-term/range correlations. However, there is a widespread belief that some stochastic or deterministic mixture of monofractals should produce multifractals [8, 19, 25]. All of them can create cascades that lie at the heart of multifractality.

Incontrovertibly, the situation is complicated. Nevertheless, we demonstrate, by studying the time series of inter-event times, that the extraction of true multifractality is possible in this crucial case. Notably, the multifractality of the series of inter-event times is poorly and only occasionally researched, although it comes from a critical role of the dependence between inter-event times. We attempt to fill the void, which is even more worrisome because inter-event or waiting times are an essential element of the modern continuous-time random walk formalism [40–42].

The use of the empirical series of inter-event times by us is of a generic nature that is, as a characteristic example of the time series for which generalized Hurst and coarse Hölder exponents have the non-monotonic behavior vs. order of scale. It is the study of the consequences of this non-monotonicity that is one of the exciting subjects of this work.

Financial markets fluctuate, sometimes strongly by increasing the risk level in order to maximize profit. This finds its reflection in the inter-event times' patterns acting as a direct reflection of the systems' activities – their various properties were studied in the last decade [1, 10, 11, 43–48]. Among them, the key observation is that quite often the dependence between waiting times dominates that between spatial increments [49] defining the process, which cannot be considered as renewal [50]. As without examining the role of inter-event times, we are not able to describe the dynamics of financial markets, these studies are still at an early stage of development. This situation is the motivation and inspiration for our work, emphasizing the above-mentioned key role of inter-event times. It is important, however, to realize that the generic goal of the work is to significantly expand the true multifractality leading to its new face, just by using the series of inter-event times as an instructive example. That is, the paper has mainly a methodological character.

B. Specific remarks

In this work, we study, for example, empirical fluctuations of inter-event times and their dependencies by relying on their absolute central moments and au-

tocorrelations of fluctuations' absolute values. In the case of financial markets, the fluctuations are (generally speaking) a consequence of the double-auction mechanism [51–53]. The approach allows you to order the fluctuations according to the degree of their corresponding moments (cf. the Lyapunov inequality in ref. [54]). It is essential in a multiscaling analysis in many branches of science.

The canonical multifractal detrended fluctuation analysis (MF-DFA) is an inspiration for our approach. However, our approach differs from it in several essential points. For example, we correctly take into account the normalized partition function (which is a non-negative one, as it should be). This partition function is built based on the normalized fluctuation function or the escort probability. Such an approach is crucial in reading from empirical data, the generalized scaling exponents. We have demonstrated that the multifractality obtained is real and not the apparent one – the latter forced mainly by too dominant finite size effect. We received the multi-branched multifractality, where the first and second-order phase transitions exist together with thermal stable and unstable phases as well. Besides, we found the left-sided multifractality for our case of empirical time series of inter-event times. Notably, it is still a challenge to find microscale physical mechanisms (or at least surrogates) underlying this multi-branched multifractality. We expect this to play a significant role in the future analysis of the real-time series of different origins e.g., geophysical, medical, and financial time series.

More specifically, the non-monotonic behavior of the generalized Hurst exponent which we found, results in turning points on the plot of the coarse Hölder exponent. It is directly responsible for the multi-branched (and left-sided in our case) spectrum of dimensions (or singularities) and for the first and second-order phase transitions, together with thermally stable and unstable multifractal phases. To the analysis of the multi-branched spectrum of singularities on the financial market (in an alternative way to that used in papers [10, 11]), the application of the Legendre-Fenchel transform is necessary. This transform is a generalization of the canonical Legendre transform routinely used to extract usual single-branched multifractality from empirical data. Besides, the slight non-monotonic behavior of the generalized Hurst exponent recently observed on the Bitcoin (BTC) market for the BTC prices [6].

It needs to be highlighted that we decided to develop a method belonging to the DFA group (see review [7] and refs. therein) and not to the coarse-graining group for reasons presented in papers [1, 55]. These papers compare the effectiveness

of MF-DFA both with Wavelet Transform Modulus Maxima (WTMM) and with Detrended Moving Average (DMA), two canonical representatives of coarse-graining methods. The ref. [1] proves, that in the majority of situations in which one does not know a priori the fractal properties of a process, choosing MF-DFA should be recommended instead of the WTMM. On the other hand, the ref. [55] proves that DMA method gives over-estimation of the Hurst exponent in comparison with DFA technique.

It is worth paying attention to one more matter. Well, when data have some intrinsic trend, the DFA methods are usually required to use. The time series of intraday inter-event times (used, for example, in this work), which play the role of noise or increments, contain this type of trend. This intrinsic trend is caused, herein, by the so-called *lunch effect* [56]. From these increments is being built the profile or walk to which you can already directly apply DFA techniques, as it was done e.g., in [1]. More specifically, the extended MF-DFA method was developed in this work, exploring the multi-branched multifractal character of long-term autocorrelated intra-day time intervals. The multi-branched multifractal is a new concept or the new face of multifractality expressed in terms of both continuous and non-continuous phase transitions.

The organization of the paper is as follows. In addition to the present section, where we give the motivation of our work and its goal, indicating a possibility of extension of our approach to research areas far beyond the social sciences, it consists of Sec. II. In this section, the expansion of the canonical MF-DFA is developed and applied to the description of poorly exploited the empirical time series of inter-event times. In Sec. III, we reveal the existence of the first and second-order phase transitions in this type of multifractality and examine the main thermodynamic consequences. Finally, in Sec. IV, we discuss critical results of the work, indicate their importance, and summarize the whole paper.

II. NORMALIZED MULTIFRACTAL DETRENDED FLUCTUATION ANALYSIS

As we said, the main subject of this work is, in fact, the analysis of true multifractality generated by the non-monotonic behavior of the generalized Hurst exponent. This non-monotonicity manifests in the multi-branch spectrum of dimensions. Besides, in our case, we found the left-sided multifractality. The central role in the analysis is, therefore, the generalized Legendre transform called the Legendre-

Fenchel transform, which also refers to as the generalized contact transform. The weak non-monotonic q -dependence of the generalized Hurst exponent was already observed in both real and spurious multi-fractality contexts in [57] (and refs. therein) – no their consequences were studied so far.

In this paper, we develop the normalized multi-fractal detrended fluctuation analysis ready for the study of both stationary and non-stationary detrended time series. It means that we allow that after detrending, time series may still contain some higher-order non-stationarities.

Our approach combines the statistical-physical analysis, based on the generalized statistical-mechanical partition function, with that based on the multiscale fluctuation function. In general, we are traveling from **absolute** moments of arbitrary orders through the partition function to multifractality. It is due to the consistent definition of escort probability introduced in Sec. II B, which is more proper than the non-normalized and sometimes even negative one given by Eq. (12) in ref. [38]. We are dealing only with the analysis of detrended absolute values, i.e., that bereft of the dichotomous noise. The motivation is that this type of nonlinear quantities can be long-term autocorrelated as opposed to the (usual) bilinear autocorrelations cluttered with noise. In our case, the autocorrelations which are studied point to the existence of a distinct antipersistent structure of fluctuations behind them. Perhaps, this structure reflects the fact that after the period of the high market activity there is a period of significantly lesser activity and so on in an alternating fashion, leading to the effect of volatility clustering.

A. Intra-day fluctuations of inter-event times: pre-processing of our formalism

The time series of inter-event times is naturally divided herein into N_d trading days or sessions, each with the same length or duration T . Besides, each session divides into s time windows, each with a length or duration Δ (s defines, herein, the daily timescale). Hence, we have $T = s \cdot \Delta$, where both N_d and T are independent of the scale s (see the schematic plot in Fig. 1 for details; in the original work [38] length Δ was marked by s . This type of division of the time series fundamentally distinguishes our approach from the MF-DFA used so far (see Appendix A for more details). Our approach does not require stapling of data from subsequent days and thus does not lead to falsification of the time series. About its important consequences, we are talking in Sec. II B. These consequences relate

only to intra-day properties of time series.

The intra-day (nonlinear) autocorrelation of the absolute additively detrended profile is defined for a single trading day (or replica) ν , $1 \leq \nu \leq N_d$, and within a timescale s ,

$$\begin{aligned} F^2(j; \nu, s) \\ = \frac{1}{s-j} \sum_{i=1}^{s-j} |U_\nu(i) - y_\nu(i)| \\ \cdot |U_\nu(i+j) - y_\nu(i+j)|, \quad \nu = 1, \dots, N_d, \quad (1) \end{aligned}$$

where dimensionless index $i = 1, 2, \dots, s$, numbers the current time window of length Δ and dimensionless index $j = 0, \dots, s-1$, defines time-step distance or number of time windows of width Δ between both absolute deviations (detrended fluctuations) $|U_\nu - y_\nu|$ present at day ν at time windows i and $i+j$; y_ν is the detrending polynomial, while quantity U_ν is defined by Eq. (3) below. As you can see, in Eq. (1) we take into account only intra-day absolute autocorrelations separately for each day. This means that polynomials are fit separately for each day, which is a major difference from the canonical MF-DFA.

Note that

$$y_\nu(i) = \sum_{m=0}^M A_\nu^m i^{M-m}, \quad M \geq 0, \quad (2)$$

wherein all our further considerations we assume $M = 3$ as it is the lowest order of the polynomial, which enables us to reproduce an inflection point present in the majority of empirical profiles, Y s, as a result of common (intraday) *lunch effect* – see the red empirical curve (small red triangles) on plot Fig. 2(b). We emphasize that this polynomial is fitted to the every-single-day (or ν^{th} day) empirical data individually. We have single-day trends, which allows analyzing single-day fluctuations constituting the foundation of this work.

Apparently, for $j = 0$ the detrended autocorrelation function (usually called in such a case the detrended self-correlation function) becomes a detrended fluctuation function. Hence, the simplified notation $F^2(\nu, s) \stackrel{\text{def}}{=} F^2(j = 0; \nu, s)$ can be used.

The single-day profile $U_\nu(i)$ for ν^{th} day at time window number i is given in Eq. (3) by the corresponding difference between subsequent multi-day profiles Y s. We assume, this difference equals the cumulation of the mean inter-event times, $\overline{\Delta t_{i'}^\nu}$, over time windows (herein indexed by i') within a single ν -day. The precise definition of this mean is given in the caption of Fig. 1.

The mean inter-event times, $\overline{\Delta t_{i'}^\nu}$, are displayed, in the form of a random comb, on plot in Fig. 2(a) (in

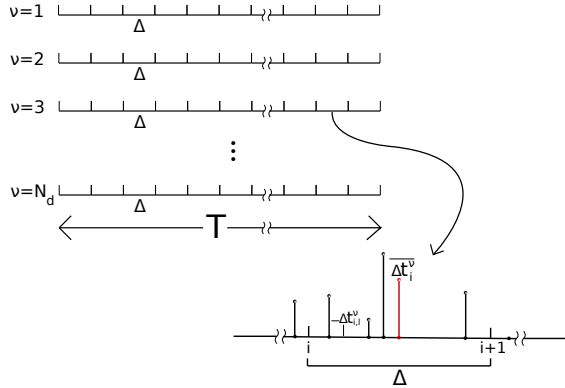


FIG. 1. Schematic diagram defining inter-event times, (local) time windows and corresponding means. Apparently, the mean for i th time window, $[i, i+1[, 1 \leq i \leq s$, (each of width Δ) is given by the corresponding time average $\overline{\Delta t_i^\nu} \stackrel{\text{def.}}{=} \frac{1}{n_i^\nu} \sum_{l=1}^{n_i^\nu} \Delta t_{i,l}^\nu$, of inter-event times, $\Delta t_{i,l}^\nu$, where $n_i^\nu \geq 1$ is the number of subsequent inter-event times belonging to time window number i and trading day number $\nu = 1, 2, \dots, N_d$. We define the inter-event time $\Delta t_{i,l}^\nu$ as belonging to i th time window $[i, i+1[$, when at least the left border of inter-event time $\Delta t_{i,l}^\nu$ belongs to it (obviously, we have $1 \leq l \leq n_i^\nu$). Additionally, we can write $\overline{\Delta t_i^\nu} \approx \Delta / n_i^\nu$, if we focus on ranges of $s \geq 1$ (keeping $n_i^\nu \geq 1$ for any i and ν).

our considerations we deal, in fact, with $\overline{\Delta t_i^\nu} \leq \Delta$). Hence, we can write,

$$U_\nu(i) = Y[(\nu-1)s + i] - Y[(\nu-1)s] \\ = \sum_{i'=1}^i \overline{\Delta t_{i'}^\nu}, \quad (3)$$

where for the first trading day ($\nu = 1$) we have $Y[(\nu-1)s = 0] = 0$ and $U_{\nu=1}(i) = Y[i] = \sum_{i'=1}^i \overline{\Delta t_{i'}^{\nu=1}}$. As you can see, the multi-day profile Y and hence the single-day U -profile are based, for simplicity, on mean inter-event times, $\overline{\Delta t_i^\nu}$, instead of inter-event times, $\Delta t_{i,l}^\nu$. In this sense, these profiles are of the coarse-grain type.

Note that, Eq. (3) makes it possible to determine the multi-day profile recurrently,

$$Y[(\nu-1)s + i] = \sum_{\nu'=1}^{\nu-1} \sum_{i'=1}^s \overline{\Delta t_{i'}^{\nu'}} + \sum_{i'=1}^i \overline{\Delta t_{i'}^\nu}, \quad \nu \geq 2. \quad (4)$$

Eq. (3) can be interpreted formally in terms of the directed (persistent or climbing) random walk – see the monotonically increasing empirical red broken curve drawn on the plot in Fig. 2(b). If there were

such a need (e.g., generalized Hurst exponent would be close to zero) it would be possible to integrate the time series before the procedure, similarly as in the canonical MF-DFA method (cf. Eqs. (7) and (8) in [38]).

Fig. 2 is intended to show the intra-day structure of empirical data, especially the absolute detrended data shown on the plot in Fig. 2(c). This plot well exhibits the leading but a bit noisy hierarchical structure of amplitudes. The levels of this structure are roughly expressed by series of $20 \times 2^0, 20 \times 2^1, 20 \times 2^2$ – the dashed horizontal lines mark its levels. The typical intra-day pattern of single-day mean inter-event times, $\overline{\Delta t_i^\nu}$, of transactions falling into the i th time window ($i = 1, 2, \dots, s$) of a given day ($\nu = 1, 2, \dots, N_d$) is shown vs i on plot in Fig. 2(a) for fixed ν ; apparently, other plots Fig. 2(b) and Fig. 2(c) are also plotted vs i . The data bursts or explosion of spikes containing hierarchy of singularities are well seen. If such a fluctuation structure was not there, we would not be able to talk about multifractality. To extract the intra-day structure of fluctuations for a given day we fitted indeed the ν -dependent polynomial $y_\nu(i)$ given by Eq. (2) (see the black curve on plot Fig. 2(b)). This approach is a more subtle than the one based on the ν -independent average over statistical ensemble of days $\langle \overline{\Delta t_i} \rangle \stackrel{\text{def.}}{=} \frac{1}{N_d} \sum_{\nu=1}^{N_d} \overline{\Delta t_i^\nu}$, which is a more coarse-grain one.

For all trading days the patterns shown on plots in Figs. 2(a) and 2(c) looks similar, although the corresponding local minima and maxima are somewhat differently distributed having slightly different amplitudes. All plots in Figs. 2 and 3 are prepared for typical time window of length $\Delta = 300$ [sec] hence, the daily total number of time windows $s = 28\ 200/300 = 94$ (as the duration of a daily stock market session of the Warsaw Stock Exchange used herein for example equals $T = 7$ [h] 50 [min] = 28 200 [sec]). It is worth mentioning that the mean number of transactions within a single time window $\Delta = 300$ [sec] is about $\langle \langle n_i^\nu \rangle \rangle = 20$ (as the empirical mean time distance between subsequent transactions equals approximately $\langle \langle \Delta t_i^\nu \rangle \rangle = 15$ [sec])). In both above given expressions internal brackets mean average over s time windows, while the external brackets mean average over N_d trading days. Thus, we introduce the averaging over both main time scales: intraday and inter-day ones. This natural two-scale division of the inter-event time series differs from that in the MF-DFA method, where the time series is treated uniformly without taking into account the division mentioned above.

It is worth noting that the local clusters of spikes

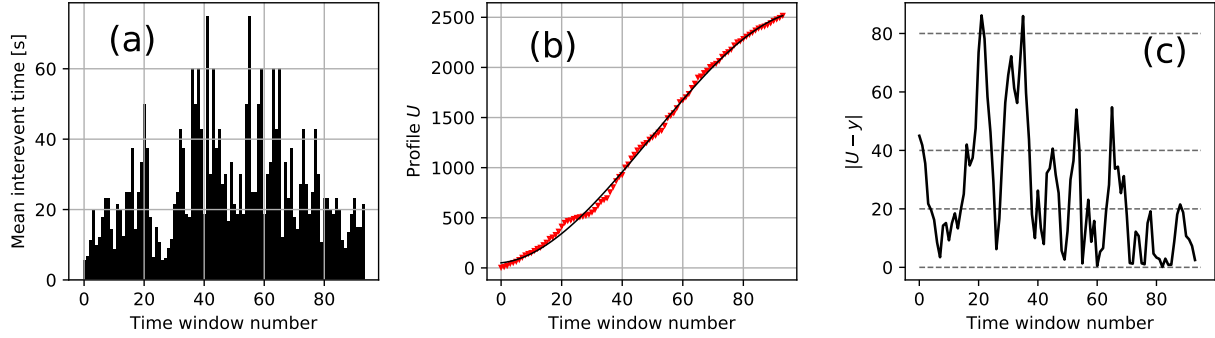


FIG. 2. Intraday patterns for the 14th January 2011 ($\nu = 9$, Friday): typical dependences of significant characteristics vs. time window number i . (a) The basic empirical quantity in the form of hierarchical comb, that is the mean interevent times $\overline{\Delta t_i^k}$, $i = 1, 2, \dots, s$ (see Fig. 1 for definition). (b) The empirical single-day profile U_ν (the monotonically increasing red broken curve is consisting of od small inverted triangles) defining a formal, directed random walk, together with the fitted smooth black curve. This latter curve represents the best fit by the third-order polynomial, y_ν , reproducing well an inflection point present in the profile. This drawing has been supplemented with the plot (c) clearly showing the fluctuating hierarchical structure of absolute deviations $|U_\nu(i) - y_\nu(i)|$ vs. i . Horizontal dashed lines mark their amplitude levels.

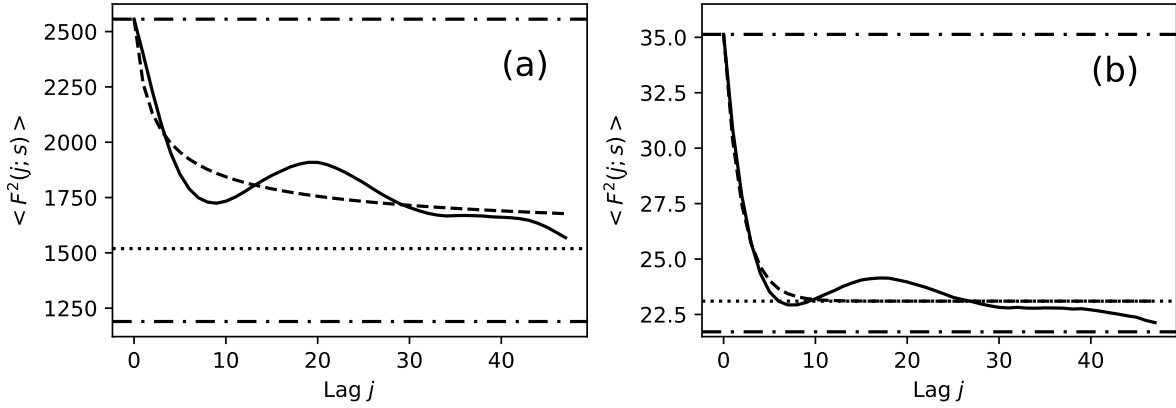


FIG. 3. The comparison of two intra-day nonlinear autocorrelation functions $\langle F^2(j; s) \rangle$ vs lag j averaged over statistical ensemble of N_d days (for instance, for $s = 94$). (a) The power-law (dashed curve) satisfactorily suites the decay of the averaged empirical autocorrelation function $\langle F^2(j; s) \rangle$ (solid curve). Note that the upper dashed-dotted horizontal line represents $\langle (U - y)^2 \rangle$, while the bottom one $\langle U - y \rangle^2$. The dotted horizontal line represents the vertical, constant shift of the power-law. Presumably, location of this autocorrelation function above $\langle U - y \rangle^2$ is due to the existence of a pattern within the time series of inter-event times (see Fig. 2 for details). The plot (b) shows the decaying of the autocorrelation function for the time-series of inter-event times generated by the Poisson process. This process is based on the empirical mean inter-event time separately for each day. The exponential function is fitted quite well here to the data (dashed curve).

around their local maximum are visible in Fig. 2(a) (to a good approximation) four times a day and not only close to lunchtime. These clusters are separated by the corresponding three of high system activity, where the shortest lengths of inter-event

times are present. Therefore, we see more or less every 100 min (= 20 time windows \times 5 min ($= \Delta$)) spikes of locally longest lengths. Such a long-term pattern constitutes one of the significant sources of a volatility clustering effect within the mean inter-

event time series. It may be the result of the existence of long-range correlations between subsequent inter-event times (cf. [58] and references therein). These correlations, presumably, can be the source of real multifractality covered herein.

As can be seen, Fig. 2 demonstrates the preparatory (first) stage of our multifractal procedure. Apparently, not only this stage differs in essence from the corresponding first stage of the MF-DFA, but as we show below, the other ones also show significant differences.

The plots in Fig. 3 present the results which are meaningful for our further considerations. It seems that the empirical autocorrelation function $\langle F^2(j; s) \rangle \stackrel{\text{def.}}{=} \frac{1}{N_d} \sum_{\nu=1}^{N_d} F^2(j; \nu, s)$ shown on plot in Fig. 3(a) is a very slowly converging (and wavy) function roughly approximated by the (shifted) power-law, $\langle F^2(j; s) \rangle = A/(a+j)^\alpha + \text{const}$ (dashed curve), where fitted shape exponent $\alpha = 0.49 \pm 0.43$ is definitely smaller than 1, fitted amplitude $A = 1049 \pm 387$, while the background parameter $\text{const} = 1519 \pm 234 > \langle U - y \rangle^2 = 1190$; hence, shift parameter $a = A^{1/\alpha} ((\langle U - y \rangle^2) - \text{const})^{-1/\alpha} = 1.0 \pm 0.90$, where $\langle (U - y)^2 \rangle = 2556$. This expression for the shift parameter is valid because we used equality $\langle F^2(j=0; s) \rangle = \langle (U - y)^2 \rangle$, which we have directly from Eq. (1) and definition of $\langle \dots \rangle$.

The slow convergence of the autocorrelation function to positive values result from its construction based on absolute values of deviations (fluctuations), which are always non-negative. Besides, its wavy behavior contains some information about the existence of a long-term fluctuation structure. We have ground to suppose that this structure is the result of the presence of the long-range correlations between fluctuations – they are the reason for the creation of this structure and not the other way round.

Besides, the autocorrelation function for the canonical Poisson process is presented (solid curve) in Fig. 3(b) as a reference case. The exponential function (dashed curve) $g(j) = A \exp(-a \cdot j) + \text{const}$ well fits the data, where $A = 12.06 \pm 0.08$, $a = 0.496 \pm 0.031$, $\text{const} = 23.12 \pm 0.08$. The fact that the dotted line does not coincide with the dashed-dotted line considers as a manifestation of the finite size effect. Because the relative difference is of the order of one percent herein, we have a reason to believe that in the case of Fig. 3(a) (where this difference is of the order of ten percent) the role of this effect is negligible. The solid curves presented on plots in Fig. 3 represent average values (over the statistical ensemble of days). Therefore, these curves obtained with higher accuracy.

One can say that the results presented in the Figs.

2 and 3 constitute the ground for the subsequent stages of the procedure.

B. Non-monotonic multiscale generalized partition function

An escort probability (that is, escorting the fluctuations) specifies the chance of occurrence of a specific fluctuation value for a given day ν within scale s . This probability constructs in the form,

$$p(\nu, s) = \frac{[F^2(\nu, s)]^{1/2}}{\text{Norm}(s)},$$

$$\text{Norm}(s) = \sum_{\nu=1}^{N_d} [F^2(\nu, s)]^{1/2} \quad (5)$$

that is, based on the fluctuation function defined by Eq. (1) for $j = 0$. Hence, the mean value, $\langle p(s) \rangle = 1/N_d \sum_{\nu=1}^{N_d} p(\nu, s) = 1/N_d$, is fixed (as a result of normalization). An even more refined approach based on a q -zooming escort probability has been shown in [61].

The generalized q -dependent or q -filtered (statistical-mechanic) partition function can be defined as usual by the sum,

$$Z_q(s) \stackrel{\text{def.}}{=} \sum_{\nu=1}^{N_d} [p(\nu, s)]^q, \quad (6)$$

where, obviously, $Z_{q=0}(s) = N_d$ and it is independent of s . This independence distinguishes our approach from the so far used multifractal analyzes. It is an important simplification of our formalism using the intraday scaling and fluctuations within the statistical ensemble of days.

We introduce the scaling hypothesis in the usual approximate form [38], which we verify in Fig. 4),

$$\sum_{\nu=1}^{N_d} [F^2(\nu, s)]^{q/2} \approx N_d A_q s^{qh(q)}, \quad (7)$$

where prefactor A_q , and the generalized Hurst exponent $h(q)$ are s -independent quantities; besides, from Eq. (7) one gets $A_{q=0} \approx 1$.

Note that scaling hypothesis (7) allowed to present $\text{Norm}(s)$ (given by the second equality in Eq. (5)) in the form

$$\text{Norm}(s) = \sum_{\nu=1}^{N_d} [F^2(\nu, s)]^{1/2} \approx N_d A_{q=1} s^{h(q=1)}. \quad (8)$$

Indeed, Sec. II C uses this expression in the critical considerations.

C. Consequences: Partial partition functions

We start this section with the introduction of reduced (relative) auxiliary quantities. It helps us define the partial partition functions that are crucial to this work.

By substituting both equalities in Eq. (5) to Eq. (6) and using hypothesis given by Eq. (7) we get,

$$\begin{aligned} Z_q(s) &\approx \frac{1}{N_d^{q-1}} A_q^{rel} s^{qh^{rel}(q)} = \frac{1}{N_d^{q-1}} A_q^{rel} s^{\tau^{rel}(q)} \\ &= \frac{1}{N_d^{q-1}} A_q^{rel} s^{(q-1)D^{rel}(q)}, \end{aligned} \quad (9)$$

where the relative (or reduced) prefactor $A_q^{rel} \stackrel{\text{def.}}{=} A_q / (A_{q=1})^q$ hence $A_{q=0}^{rel} \approx 1$, $A_{q=1}^{rel} = 1$, the relative (or reduced) generalized Hurst exponent $h^{rel}(q) \stackrel{\text{def.}}{=} h(q) - h(q=1)$ is vanishing at $q = 1$, and the relative (or reduced) scaling exponent $\tau^{rel}(q) \stackrel{\text{def.}}{=} qh^{rel}(q)$ is vanishing at $q = 0$ and 1. Having a well-defined reduced scaling exponent, we introduce a formal analog of Rényi dimensions, $D^{rel}(q) = \tau^{rel}(q)/(q-1)$, that is relative (reduced) ones, vanishing at $q = 0$. As you can see, in this representation you do not need any information about the Hausdorff dimension of the time series support. The information $D^{rel}(q=1)$ and correlation $D^{rel}(q=2)$ dimesions have formally the same forms as the corresponding canonical Rényi dimensions (see Appendix B for details).

Finally, we can write Eq. (9) in the form of the product of the partial partition functions, key for our further considerations,

$$Z_q(s) \approx \frac{1}{N_d^{q-1}} A_q^{rel} s^{\tau^{rel}(q)} = Z_q^{lin}(s) \tilde{Z}_q(s), \quad (10)$$

here

$$\begin{aligned} Z_q^{lin}(s) &= \frac{1}{N_d^{q-1}} A_q^{rel} s^{-(q-1)D(q=0)}, \\ \tilde{Z}_q(s) &= s^{\tau(q)}, \end{aligned} \quad (11)$$

where we have to define

$$D(q=0) \stackrel{\text{def.}}{=} h(q=1) \quad (12)$$

for self-consistency (without more profound analysis of this fact), while scaling exponent

$$\tau(q) \stackrel{\text{def.}}{=} qh(q) - D(q=0). \quad (13)$$

The quantity $D(q=0)$ requires a comment.

D. Interpretation of $D(q=0)$ in the frame of our formalism

In the canonical MF-DFA approach, one can read directly from the scaling relation for the partition function that $D(q=0)$ is the support's Hausdorff dimension for the time series – usually $D(q=0) = 1$.

Since in our approach, the Rényi dimensions enter into the generalized partition function on a relative way, such a diagnosis does not take place. Therefore, $D(q=0)$ does not have to be a fractal dimension of the substrate (and $D^{rel}(q=0)$ even vanishes). The knowledge of $D(q=0)$ does not require its value to take independently outside our formalism. It is designated by the information Hurst exponent $h(q=1)$ – it is related to information and not topology. For this reason, the $D(q)$ family should rather be called pseudo Rényi dimensions, while $D^{rel}(q)$ family of the relative or reduced one despite the fact that for $q \neq 0$ both families have the usual interpretation formally (see Appendix B for details). However, in the further part of the work, we return to the simplified name ‘Rényi dimensions’ for $D(q)$ remembering, of course, the above-given conditions.

Using the scaling exponent τ , we can define now the Rényi dimensions in the usual way

$$D(q) \stackrel{\text{def.}}{=} \frac{\tau(q)}{(q-1)}, \quad (14)$$

which additionally allows to present D^{rel} in the reduced form $D^{rel}(q) = D(q) - D(q=0)$. Notably, all the relative quantities defined above (and indexed by ‘rel’) disappear in either $q = 0$ or/and in $q = 1$, which results from their relative character.

The partial partition functions Z_q^{lin} and \tilde{Z}_q are normalized separately, and the factorization given by Eq. (10) (up to multiplicative prefactor and additive exponents) is unique. These partition functions represent statistically independent monofractal and multifractal structures, respectively. We pay attention to the most interesting the latter one.

E. Legendre-Fenchel transformation and multi-branched left-sided multifractality

In this section, we carry out our multi-branched multifractal analysis on the example of the time series of inter-event times.

Directly from Eq. (7) we obtain,

$$\ln \mathcal{F}_q(s) \approx h(q) \ln s + B(q), \quad (15)$$

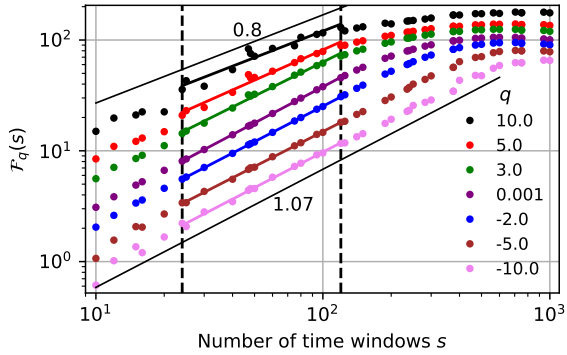


FIG. 4. Plots of function $\mathcal{F}_q(s)$ (defined by Eq. (16)) vs. s within the log-log scale for different values of $-10 \leq q \leq 10$. Vertical dashed lines define the common region of the best fit of all straight lines and they are located the first one at $s = 24$ or 19 min 35 s and the second one at $s = 120$ or 3 min 55 s. The upper and lower thin black straight lines define the boundaries in which the slope of the fitted lines is included herein, between 0.80 and 1.07, still far beyond statistical errors.

where q -dispersive

$$\mathcal{F}_q(s) \stackrel{\text{def.}}{=} \left\{ N_d^{-1} \sum_{\nu=1}^{N_d} [F^2(\nu, s)]^{q/2} \right\}^{1/q} \quad (16)$$

and $B(q) \stackrel{\text{def.}}{=} q^{-1} \ln A_q$.

Using the dependence of $\mathcal{F}_q(s)$ on the scale s (see Fig. 4 for details) for values of q from its wide range (that is $-10.0 \leq q \leq 10.0$), we have determined both the generalized Hurst exponent $h(q)$, its spread $\Delta h(q) = h(-q) - h(q)$, significant prefactor $B(q)$ present in Eq. (15) related to reduced Rényi information, related signatures of multifractality such as Rényi scaling exponent $\tau(q)$, Rényi dimensions $D(q)$, and the coarse Hölder exponent $\alpha(q)$ (see plots in Fig. 5 for details). Let us emphasize that all these quantities, together with multifractal spectrum $f(\alpha)$ considered below, and their standard deviations were obtained from empirical data directly or indirectly thanks to Eq. (15).

By taking the scaling exponent $\tau(q)$ from Eq. (13), the coarse Hölder exponent $\alpha(q)$ and multi-branched multifractal spectrum $f(\alpha)$ can be found. We define below the Legendre-Fenchel (LF) transformation instead of Legendre transform. Although formally both look the same, the former allows a

multi-branch solution. We have,

$$\begin{aligned} \alpha(q) &\stackrel{\text{def.}}{=} \frac{d\tau(q)}{dq}, \\ f(\alpha) &\stackrel{\text{def.}}{=} q\alpha(q) - \tau(q), \end{aligned} \quad (17)$$

hence,

$$q = \frac{df(\alpha(q))}{d\alpha} \text{ and } f = -\frac{d(\tau(q)/q)}{d(1/q)}, \quad (18)$$

where α is a local dimension (singularity or coarse Hölder exponent – its q -dependence is shown in Fig. 5(f)), while $f(\alpha)$ is its distribution shown on plots Fig. 6(a) and Fig. 6(b). As usual, for the monofractal structure the scaling exponent $\tau(q)$ is a linear function of q , while for multifractal it is a non-linear one.

From Eq. (13) and the second equality in Eq. (17) we obtain the expression $\alpha(q) = h(q) + q \frac{dh(q)}{dq}$. This means that at $q = 0$ and $q = q_{extr}$ we obtain $\alpha(q) = h(q)$, where q_{extr} defines q -position of a local extremum of h function; however, it does not mean the extremum of $\alpha(q)$ function.

It is worth emphasizing that aggregating events into time intervals of the same length (Δ , see Fig. 1 for details) may influence the analysis. Namely, if the intervals are too short concerning the average waiting time between consecutive events, then too many of them will be empty. On the other hand, if the intervals are too long, aggregation of too many points may lead to loss of information on the time structure of the process.

Indeed, the analysis shown in Fig. 4 proposes a solution to this problem, showing that the appropriate range of Δ is the one in which the scaling effect is observed, herein on $\mathcal{F}_q(s)$ vs $s = T/\Delta$, where $T = 7$ h 50 min or 470 min and for all values of q we have a common range 3 min 55 s $\leq \Delta \leq$ 19 min 35 s. For this range of s , the measure χ^2 per degree of freedom reaches the smallest value. Only slightly larger is this quantity when the left border of s is assumed to be $s = 10$ or $\Delta = 47$ min, while the right one is $s = 150$ or $\Delta = 3$ min 8 s.

It must be clearly stated that due to the non-monotonic dependence of the generalized Hurst exponent $h(q)$ versus q , spectrum of dimensions $f(\alpha)$ is the multi-branched function of the Hölder α exponent (see plots Fig. 6(a) and Fig. 6(b) for details).

Recall that the Legendre transformation deals only with monotonous functions $h(q)$. From this point of view, Eqs. (17) and (18), although formally identical to the Legendre transform, are its generalization. The Legendre transform is limited here only to the main branch of spectrum f defined by its contact relations:

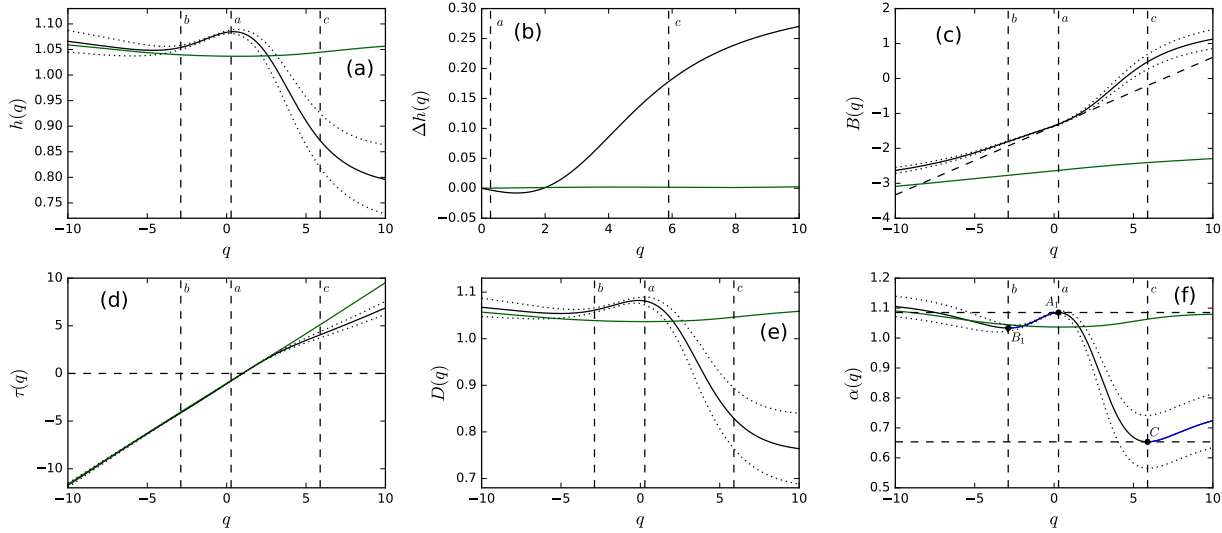


FIG. 5. We present the q -dependence of key empirical characteristics of multifractality. The nonlinear dependence of these characteristics on q we show on all plots (black curves, while dotted curves designate corresponding one-standard-deviation bands; in addition, fragments $[B_1, A_1]$ and that starting from point C of the curve $\alpha(q)$ are blue). Plots (a) – (f) present dependence on q of the generalized Hurst exponent $h(q)$, its spread $\Delta h(q) = h(-q) - h(q)$, prefactor $B(q)$ related to reduced Rényi information, Rényi scaling exponent $\tau(q)$, Rényi dimensions $D(q)$, and the coarse Hölder exponent $\alpha(q)$, respectively. The straight vertical dashed lines a and c define the range of q -support located between the absolute maximum A_1 and absolute minimum C of curve $\alpha(q)$ shown in plot (f) vs q . The similar line b indicates the location of the second minimum B_1 of the curve $\alpha(q)$. The mentioned lines we also applied to the remaining plots. The tangent dashed straight line visible in the plot (c) we fitted to the linear section of curve $B(q)$ vs. q . Additional thin (green) solid curves present on all plots we obtained from the time series (of the same size as the empirical ones) generated by the Poisson distribution. Their variations are negligible. It means that the influence of a finite size effect on a time series with a size equal to the empirical one is irrelevant.

$$(i) f(\alpha(q=1)) = \alpha(q=1)$$

$$(ii) \frac{df}{d\alpha(q)}|_{\alpha(q=1)} = 1.$$

The inset plot present in Fig. 6(b) illustrates this contact character. This is emphasized by a dashed straight line with directional coefficient (slope) of 1.0 tangent to spectra of singularities at the point $[\alpha(q=1), f(\alpha(q=1))]$. Breaking the contact character of the Legendre transformation results in the wrong location of the spectrum of singularities if it exists.

Put more generally, the given contact relations above (for $q = 1$) provide the unambiguous location of the full multi-branched spectrum of dimensions obtained using the Legendre-Fenchel transformation. Our multi-branched multifractal contains a single contact point which means that we are dealing here with the single multi-branched multifractal. Fig. 6(a) and Fig. 6(b) shows a significant result because it offers a necessary (not sufficient) requirement for finding true multifractality in empirical time series.

Thanks to the above, we can clarify the key term *multi-branched left-sided multifractality*. We say that we are dealing with this type of multifractality if its main branch (that is, the branch that meets the condition of contact) is fully determined only by the positive values of q . It is our situation, which is visible, thanks to Fig. 5(f) depicting the relationship between α and q .

III. FIRST AND SECOND ORDER PHASE TRANSITIONS

The multi-branched left-sided multifractality obtained by us results in a fundamental thermodynamic consequence. Studying this type of impact is the standard way to analyze the properties of multifractals. The indicator of their classification is specific heat of the multifractal structure [11] (and refs. therein).

From Eq. (17) one can obtain a useful expression for the specific heat of the multifractal structure in

the form,

$$c(q) = \frac{d\alpha(q)}{d(1/q)} = -q^2 \frac{d\alpha(q)}{dq}; \quad (19)$$

its q -dependence is shown in Fig. 6(c).

Only two regions are visible in which the system is thermally stable, i.e. fulfilling inequality $c(q) \geq 0$ (or $\frac{d\alpha(q)}{dq} \leq 0$). The first of them is located between vertical dashed straight lines a and c or points A_1 and C (the same as shown in Fig. 5). Thus, we defined the q -range of the main branch of the left-sided spectrum of dimensions limited correspondingly by the same dashed lines and points. All of them we show in Fig. 6(a) and Fig. 6(b) (related to the monotonically increasing black curves on both plots). The second region is limited to the range of q preceding vertical dashed straight line b presented on plots Fig. 5(a), (c)–(f) or point B_1 on plot Fig. 5(f). In this way we get q -support of the side-branch spectrum of dimensions (the decreasing black curves in plots Fig. 6(a) and Fig. 6(b)). Moreover, between points X_1 and X_2 located in thermally stable phases (see Fig. 6(b)), the first-order phase transition occurs. It is considered below in the context of Fig. 7.

A peculiar characteristic of our multifractal is the presence of negative spectra of dimensions, in the vicinity of the turning point C , in Fig. 6(a), which could be justified by the appearance of events that occur exceptionally rarely (see [17] for some suggestions).

We deal with thermally unstable phases for the opposite case $c(q) < 0$ (or $\frac{d\alpha(q)}{dq} > 0$). They range between turning points B_1, A_1 and after point C , presented in Fig. 5(f) and Fig. 6(c). In Fig. 6(b) this range of q is clearly visible. It is the q -support of the bifurcating branch of our multi-branched multifractal (the solid blue curve stretching between points B_1 and A_1 ; in Fig. 6(a) the highest placed short blue curve represents it stretched between dashed vertical lines a and b). In points B_1, A_1 , and C , there are phase transitions of the second-order between thermally stable and unstable phases, which is consistent with specific heat vanishing there. It is discussed below in the context of Fig. 7 (together with a description of the role of points D_1 and D_2).

To prove the above given statements concerning the order of phase transitions, we study the behavior of the first, $df/d\alpha$, and second, $d^2f/d\alpha^2$, derivatives Ivs α , based on the result presented in Fig. 5(f). Using the Taylor expansion of $\alpha(q)$ function in the

vicinity of its local extremes we obtain,

$$\alpha(q) \approx \alpha(q_{extr}) + \frac{1}{2}(q - q_{extr})^2 \frac{d^2\alpha}{dq^2} |_{q=q_{extr}}, \quad (20)$$

where q_{extr} is a q -position of the local extreme or turning point of $\alpha(q)$ function. There are three such local extremes: one maximum A_1 and two minima B_1, C .

Inverting Eq. (20) and using the first equation in (18), after simple algebraic calculations, we obtain useful two-branched formulas,

$$\begin{aligned} \frac{df}{d\alpha} &\approx \pm \sqrt{2 \left| \frac{\alpha - \alpha_s}{\ddot{\alpha}_s} \right|} + q_{extr}, \\ \frac{d^2f}{d\alpha^2} &\approx \pm \frac{1}{\sqrt{2 \left| \ddot{\alpha}_s \right|}} \frac{1}{\sqrt{\left| \alpha - \alpha_s \right|}}, \end{aligned} \quad (21)$$

where we use the abbreviated notation: $\alpha_s = \alpha(q_{extr})$ and $\ddot{\alpha}_s = \frac{d^2f}{d\alpha^2} |_{q=q_{extr}}$. Apparently, spectrum of dimensions f has singularities of the second order at its turning points (see Fig. 6(a), Fig. 6(b), and Fig. 7 for illustrating).

Moreover, by substituting the expansion given by Eq. (20) to Eq. (19), we obtain

$$c(q) \approx -q^2(q - q_{extr})\ddot{\alpha}_s, \quad (22)$$

i.e., it linearly vanishes at turning points, which can be considered to be spinodal decomposition points (see Fig. 7 for details).

Fig. 7 shows the behavior of the first ($df/d\alpha$) and second ($d^2f/d\alpha^2$) order derivatives of spectrum of dimensions (f) versus Hölder exponent (α). In combination with the plots (a) and (b) in Fig. 6, this allows us to classify phase transitions at points A_1, B_1 , and C and at a point marked twice by X_1, X_2 .

The modified Ehrenfest or Mandelbrot classification of phase transitions which we consider is based on the spectrum of dimensions f , which we treat as the analogon of entropy [8, 11]. Therefore, the classification suggested by Mandelbrot [12, 13] can be considered only as inspired by the Ehrenfest one – the latter classification uses the chemical potential and not the entropy, although both quantities are functions of the thermodynamic state of the system. The Mandelbrot classification is by one order of magnitude lower than the Ehrenfest classification – this is because the entropy is a partial derivative of the chemical potential. The use of Mandelbrot classification in the case of multifractals is more convenient from a technical point of view since entropy is obtained here directly from the LF transformation given by Eq. (17) in contrast to the chemical potential.

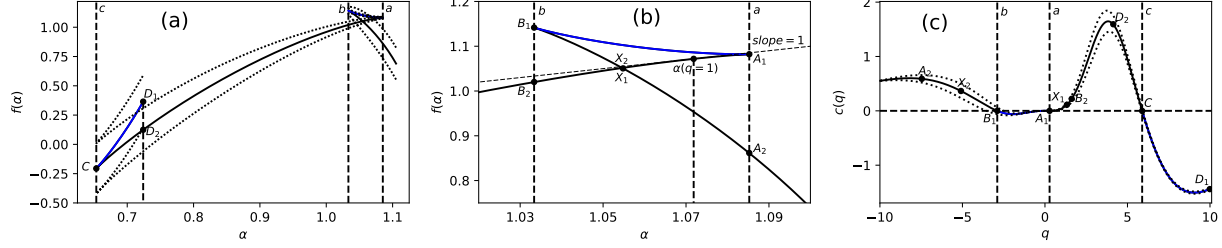


FIG. 6. Two plots (a) and (b) (the latter gives the enlarged part of plot (a)) show complementary views of spectrum of dimensions $f(\alpha)$ (given by Eq. (17)) vs α . On these plots the main branch of spectrum $f(\alpha)$ is presented by the increasing black curve. Plot (c) presents the specific heat $c(q)$ (given by Eq. (19)) vs q , which allows you to clearly define thermal stable and unstable phases. The vertical dashed straight line displayed on the plot (b) in point $\alpha(q=1)$, determines the position of the tangent dashed straight line with a slope of 1.0 for the main branch. It is a verification of the contact [property](#) of the L-F transform. Other dashed lines are described in the main text, while a pair of points X_1, X_2 and D_1, D_2 in the context of Fig. 7 below. The dotted curves designate corresponding one-standard-deviation bands.

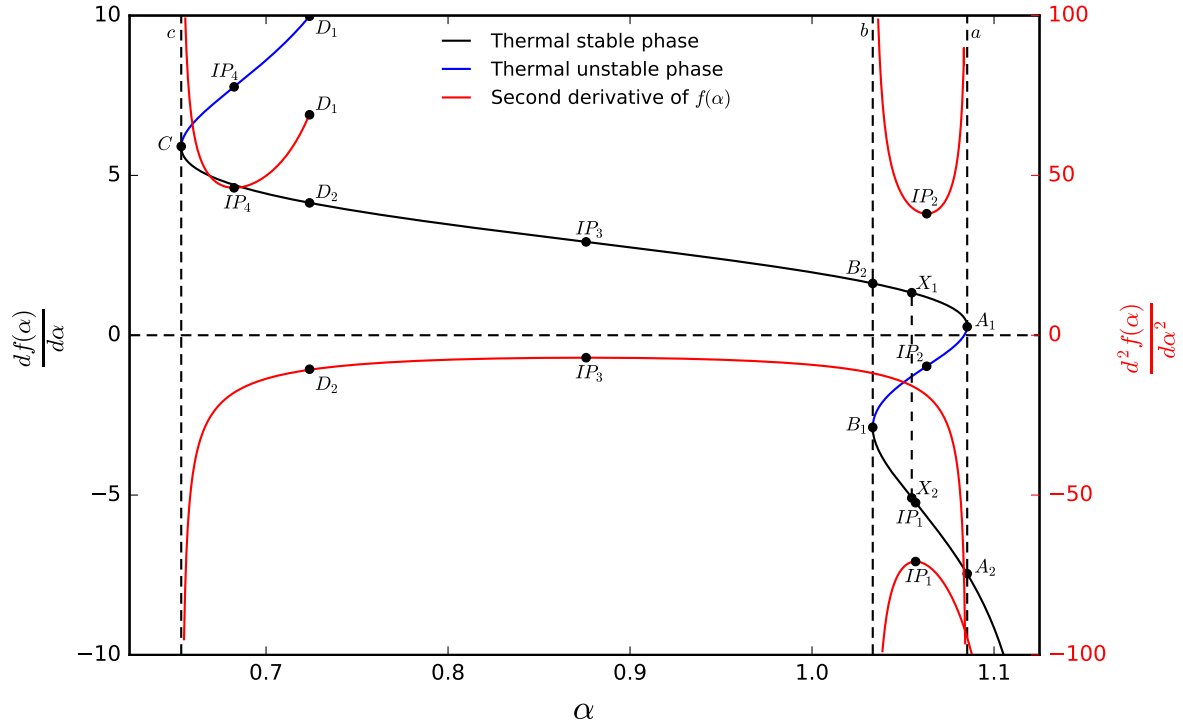


FIG. 7. The schematic illustration of the modified Ehrenfest or Mandelbrot classification of phase transitions [66]. The first (black and blue fragments of a single solid curve) and second (four separated red solid curves) order derivatives of f over α showing three two-branched second-order singularities of f vs. α . Three dashed vertical straight lines (vertical asymptotics) c, b , and a are located, at α coordinates of these singularities. In the main text of this section, we provide an exact discussion of this figure.

Apparently, f and $df/d\alpha$ are the continuous functions of α as opposed to $d^2f/d\alpha^2$ (see Figs. 6 and 7 for details) – both derivatives are calculated numerically as numerical dependence $f(\alpha)$ from α is known (cf. Fig. 6). All these functions are multi-branched but only the second order derivative consists of separated branches (cf. red curves in Fig. 7).

All these separated branches except one diverge asymptotically to $\pm\infty$ just in turning points A_1, B_1 , and C (the corresponding vertical asymptotics denoted by the dashed lines a, b, c are presented in Fig. 7 and also in Figs. 5 and 6). These asymptotic divergences happen according to the power-law with an exponent equal to $-1/2$ – see the second equality in Eq. (21). It means that in these points, there are identical phase transitions of the It second order according to our classification i.e., belonging to the same universality class) – this confirms the behavior of specific heat given by Eq. (22). That is, at the points of the second-order phase transition the specific heats, susceptibilities or other appropriate order parameters either diverge (obeying a non-trivial scaling law) or go to zero – the latter case happens in our situation (cf. Fig. 6(c)).

The main branch of derivative $df/d\alpha$ is represented by the black curve (C, D_2, B_2, X_1, A_1) containing the inflection point IP_3 (the corresponding curve on Fig. 5(f) has a less detailed description). The corresponding second order derivative $d^2f/d\alpha^2$ (red curve containing the replica of point D_2 and inflection point IP_3) diverges to $-\infty$ at asymptotics c and a . Therefore, this curve is singular at turning points: its left arm at α coordinate of point C and the right one at α coordinate of point A_1 .

The other three separated singular curves (also in red) are associated with three side branches of the first-order derivative df/α . The most upper one (located in the left part of the figure, ending at the replica of point D_1), has its local minimum at a replica of the inflection point IP_4 . This curve is bound to side branch (C, D_1) (short blue curve) of the first derivative, containing the inflection point IP_4 . This branch is thermally unstable (see the plot in Fig. 6(c) for details) as heat capacity is negative. The upper curve (placed at the right part of the figure), having its local minimum at the replica of inflection point IP_2 (also marked by IP_2), is bound to branch (A_1, IP_2, B_1) (short blue curve) of the first-order derivative, where points A_1 and B_1 we consider as spinodal decomposition points – there is a thermally unstable territory between them (see plot in Fig. 6(c) for details again). The third singular solid curve, having its local maximum at a replica of inflection point IP_1 (also denoted by IP_1), is bound to branch (B_1, IP_1, A_2) . Its left branch has asymptotics at point B_1 , while its right branch has no asymptotics at the point A_2 .

Of course, all branches of the first derivative we associate with the corresponding branches of the spectrum of dimensions, f vs. α , clearly shown on plots Fig. 6(a) and Fig. 6(b).

Let us note that short black (X_1, A_1) and (B_1, X_2) curves define the thermally metastable phases, while the short blue curve (A_1, B_1) defines the unstable mixture of phases – those phases that are described by the black B_2, X_1, A_1 and B_1, X_2, A_2 curves. If the system locates in a mixture phase, it will spontaneously evolve towards a state, which favors either higher fluctuations (defined by q larger than that for point A_1) or smaller fluctuations (defined by q lower than that for point B_1). The probability of choosing one of these two options depends on how closely the state of the system locates near the edge of the phase.

For the unstable phase defined by the short blue curve (C, D_1) containing the inflection point IP_4 , a simplified interpretation we develop. It is because we did not locate it between two metastable phases, although $d^2f/d\alpha^2$ diverges at transition point C in the same way as at points A_1 and B_1 . We can only say that the system left alone in this phase will spontaneously evolve into the stable phase.

In Fig. 7 we present the first-order (discontinuous) phase transition between single phases by the short vertical dashed line connecting X_1 and X_2 points. Notably, in Fig. 6(b) this first-order phase transition point is marked twice by X_1 and X_2 – this defines a single point of branch intersection. We can explain it in the sociological terms. In the mixture phase region, the members' moods/opinions divide, and the victory of one of them may lead either to a permanent increase in the diversity of the members' moods/opinions of the system or to their lasting calm.

IV. CONCLUDING REMARKS

Our work belongs to the research on the problem of long-term dependence, long-term memory, and long-term/range correlations in time series. [65]. By using the Legendre-Fenchel (or generalized Legendre) transform we have examined, the resulting multi-branched left-sided non-spurious or real multi-fractal properties of time series of inter-event times. We have chosen inter-event times for our research because they are a crucial measure of the activity of many systems (not necessarily complex) – the research into which is only at the initial stage. The relationships between inter-event times form the foun-

dation of other dynamic relationships occurring in an evolving system. The time series of inter-event times has led to the non-monotonic behavior of the generalized Hurst exponent – the principal one for our study.

Our research focuses on the search for multifractality because it is the most general, as of yet, characterization of time series at a macro scale, enabling the study of their universal properties from an extended point of view (allowing their classification by using their singularity spectra or spectra of dimensions). However, deriving a microscopic model from the knowledge of the multifractal structure of series of inter-event times is still under consideration. A step toward this direction we proposed in [11], where the surrogate model was the CTRW with waiting-time distribution weighted by stretched exponential i.e., defined by some superstatistics. It is an approach sufficient to describe multifractality generated by a broadened distribution, but in the case of multifractality caused by long-term autocorrelations of inter-event times, it is still a significant challenge.

As is known, the search for nonspurious/true multifractality first requires the resolution of the role of at least the main factors: (i) main non-stationarity, (ii) finite size effect, and (iii) broadened distribution sometimes leading to non-spurious and unfortunately, to spurious multifractality. The detrending procedure described in Sec. II A solved point (i) , while points (ii) and (iii) are vividly illustrated in Fig. 8, where the Rényi scaling exponent $\tau(q)$ is presented for three characteristic cases.

The blue (almost) linearly increasing the solid curve shown in Fig. 8 we obtained from the Poisson distribution. For this distribution, we have drawn several transactions in each time interval (numbered by index i), and on this basis, the local mean time of inter-event times, $\overline{\Delta t_i^p}$, is determined (see Fig. 1 for a detailed analysis). These local mean times create a time series with a size equal to the whole empirical time series of inter-event times. We achieve this by introducing a limitation that the last element (inter-event time) of the time series must cut so that the entire synthetic time series is equal to the number of days N_d multiplied by the length of a single session $s \cdot \Delta$. The presence of possible spurious multifractality here is caused only by the finite size of the time series of inter-event times of the same size as the empirical time series. The spurious multifractality of the Poisson time-series caused only by finite-size effect is negligible in this case as $\tau(q)$ is (almost) a linear function of q . Therefore, we can expect the influence of the finite size effect on real multifractality also negligible. The finite-size effect is subtly treated below for the red curve in Fig. 8.

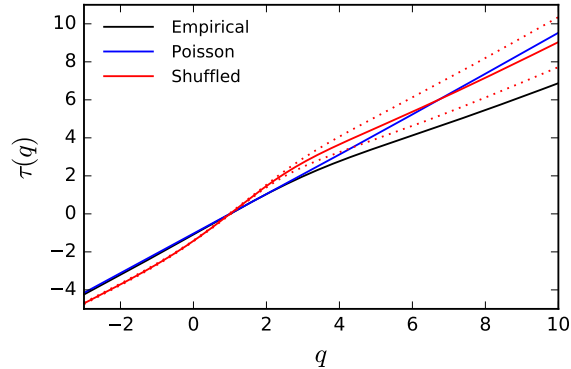


FIG. 8. Comparison of three particular types of Rényi scaling exponent $\tau(q)$ vs. q . (i) The black solid curve (taken from Fig. 5(d)) obtained directly from empirical time series of inter-event times by using our NMF-DFA. (ii) The blue (almost) linearly increasing solid curve we derived from the Poisson distribution. (iii) The solid red curve bases on the shuffled empirical inter-event time series. The red dotted curves define its one-sigma corridor, where sigma is a standard deviation.

However, the origin of the solid red curve in Fig. 8 needs an explanation. We create it in the following three steps.

- (i) We construct the statistics from the empirical series of inter-event times.
- (ii) A new time series is drawn from the statistics thus built. This series can be called a shuffled time series. Please note that the duration of the session limits this draw. Thus, we trim the last inter-event time on a given day so that this condition meets. It is done for each day (session) separately. Perhaps this condition alone is the reason for the slight waving of the red curve in Fig. 8. In this way, all-time correlations are destroying (except for the above-mentioned small waving of the red curve) if time series was sufficiently long.
- (iii) Finally, the exponent $\tau(q)$ is determined from this shuffled time series by the NMF-DFA.

Solely, the black solid curve (presented in Fig. 8) obtained from empirical time series of inter-event times by using the NMF-DFA, is sufficiently non-linear to generate multifractality.

Thus we show, by using the NMF-DFA, that an empirical series of the inter-event times gives a true multifractal located far beyond the finite size component and other multifractal pollutions. We sug-

gest that the long-term autocorrelations between absolute values of detrended inter-event time profiles caused herein the real multifractality. These autocorrelations create some true antipersistent structure of fluctuations' clusters of the inter-event times, seen clearly in Fig. 2(c) and Fig. 3(a), defining the volatility clustering effect. Interestingly, intraday empirical data are sufficient to detect true multifractality, even though the autocorrelations of the inter-event times mentioned are long-term, stretching presumably for many days.

This work bases on two main pillars. First of all, on the NMF-DFA approach constructed in work, which was inspired by the canonical MF-DFA. Thanks to the NMF-DFA approach, it has been proved that the time series of inter-event times can have a multi-branched left-sided multifractal character. Secondly, the work demonstrates that this type of multifractality can lead to phase transitions of the first and second orders according to the Mandelbrot classification. We want to draw attention to the high similarity of both phase transitions to the corresponding phase transitions of the first and second orders according to the Ehrenfest classification.

For the traditional multifractality, the phase transition of the first order disappears, which reduces the area of metastable and unstable phases to zero. It means that canonical multifractality corresponds to critical or supercritical states of the system. Thanks to this, we better understand why long-term correlations play a crucial role in the building of multifractality. In this situation, the details of microscopic models leading to this type of multifractality do not represent a significant role. From this point of view, the multifractality presented in this work is subcritical, where stable, metastable, and unstable phases are still present. From the level of this work, traditional multifractality can be treated only as one of the elements of full classification. Thanks to this, the concept of multifractality has been broadened substantially.

ACKNOWLEDGMENTS

The authors are grateful for stimulating discussions with S. Drożdż, D. Grech, and P. Oświęcimka.

Appendix A: Pre-processing and coarse-graining

We compare the coarseness used in pre-processing of our approach with seminal Kantelhardt et al. one [38], emphasizing the differences between both.

In both approaches the length of the time series (i.e., the number of points or empirical data) is determined once and marked herein by the product $T \cdot N_d$, where T is the fixed, daily length of the time series (resulting from the duration of the session) and N_d is the set number of days/sessions. The scale s , the same for each day, is introduced by equality $T = s \cdot \Delta$, where Δ is the length of the sub-segment and s the number of these sub-segments. Thus, two separated time scales are present here: one defined by s and the other by N_d . It is a different approach than the one presented in Kantelhardt's et al. work [38].

Our approach distinguishes between individual sessions (each with the same duration of T) as opposed to the method of Kantelhardt et al. [38]. This distinction is natural, and we cannot ignore it. For example, our approach allows you to distinguish possible jump of quotation at the opening of each session. In general, this may be different from intra-sessional (intraday) jumps. The approach of Kantelhardt et al. equates inter-sessional with intra-sessional jumps – it does not make it possible to distinguish them. It loses a piece of information that is perhaps important, and we cannot mask it. It has its consequences in multi-scale divisions of the time series.

Figs. 1 in Kantelhardt et al. and our works illustrate the way of introducing scales in both approaches. In the approach of Kantelhardt et al. there is a division of the time series into subsegments of length s each (this s is different from the one used by us). Hence, we have $N_s = [N/s]$ such segments, where [...] means truncation to a natural number. These segments are detrended individually, which leads (most often) to the non-physical jumps of the trend (frequently massive) on the borders of subsegments.

Our approach is devoid of the abovementioned disadvantage, as detrending is conducted for each session separately. The possible trend jump at the opening of each session is here consistent with the spirit of quotations allowing such increases. No other trend jumps occur in our approach. There is no separate detrending inside any interval Δ , only detrending the entire session. Such an approach does not destroy or remove any fluctuations, nor does it produce artifacts in the form of changes.

Of course, the way the scale we introduce is the crucial element of both approaches. As you can see, we enter the concrete scale through sub-segments with a length of Δ or (equivalently) through their number of s . Inside each Δ subsegment, we build the time average of interevent time intervals. That is, we replace the intra-segment detrending present in the

approach of Kantelhardt et al. through an intra-segment average and one-session detrending. One-session detrending now detrends a series of these (local) average values, removing intra-day leading non-stationarity i.e., lunch effect. Of course, the Δ is larger, the time distances between these average values increase, and we see fewer and fewer details in the revised signal. It is similar to observing, for example, a suspension under a microscope. If the magnification is insufficient, then we see a blurred image averaged, although the shape of the picture (that is its essential feature) is still recognizable. Increasing the magnification (i.e., reducing Δ) we see more and more details – the shape of the image does not disappear but is more abundant with more information and sharpened. In other words, the operation of the abovementioned mean values is natural and does not destroy the essential features of the time series.

Notably, the average of the power-law dependence within the Δ interval does not change its exponent as long as it is at most a slowly-changing function of variable x and $\Delta \ll x$. These results from the following simple integration,

$$\begin{aligned} \frac{1}{\Delta} \int_x^{x+\Delta} \frac{1}{y^{1+\alpha}} dy &\propto \frac{1}{\Delta} \frac{1}{x^\alpha} \left(1 - \left(1 + \frac{\Delta}{x} \right)^{-\alpha} \right) \\ &\approx \frac{1}{\Delta} \frac{1}{x^\alpha} \left(1 - \exp \left(-\alpha \frac{\Delta}{x} \right) \right) \approx \frac{\alpha}{x^{1+\alpha}}. \end{aligned} \quad (\text{A1})$$

In addition, the time series consisting of the average values (built independently in each time window of width Δ) does not lose fluctuations but only decreases their amplitude by the standard factor $\sqrt{n_i^\nu}$, which is at most of the order of ten in our case, where dimensionless index $\nu = 1, 2, \dots, N_d$ numbers trading days, while dimensionless index $i = 1, 2, \dots, s$, numbers time windows wherein all time windows have the same width Δ and their amount (the same for each day) is equal to s .

Appendix B: Properties of the multi-branched multifractal

In this section, we consider the chosen characteristics of multifractality at some significant values of q .

1. Case $q \rightarrow 0$

This case fundamentally distinguishes our multi-branched multifractality from the ordinary single-branched multifractality. Our approach is unified

– it is entirely based on the generalized Hurst exponent. From Eqs. (6), (10) – (13) we obtain $\tau(q = 0) = -D(q = 0) = -h(q = 1)$ (see also Fig. 5(d) for details), where we took advantage of the fact that generalized Hurst exponent is finite. You can see that the scaling exponent is controlled at $q = 0$ only by the generalized Hurst exponent at $q = 1$, which has nothing to do with the support of the time series.

2. Case $q \rightarrow 1$: Shanon information

In this case one can write the expansion,

$$\begin{aligned} \tau(q) &\approx (q - 1)[h(q = 1) + q \frac{dh(q)}{dq} |_{q=1} \\ &\quad + \frac{1}{2} q(q - 1) \frac{d^2 h(q)}{dq^2} |_{q=1}], \end{aligned} \quad (\text{B1})$$

based on the expansion of $h(q)$ in the vicinity of $q = 1$, where the expression in square brackets is indeed,

$$\begin{aligned} D(q) &\approx D(q = 0) + q \frac{dh(q)}{dq} |_{q=1} \\ &\quad + \frac{1}{2} q(q - 1) \frac{d^2 h(q)}{dq^2} |_{q=1} \end{aligned} \quad (\text{B2})$$

that is, the expansion of Rényi dimensions in the vicinity of $q = 1$.

Equivalently we have,

$$\begin{aligned} \tau^{rel}(q) &\approx (q - 1)[q \frac{dh(q)}{dq} |_{q=1} \\ &\quad + \frac{1}{2} q(q - 1) \frac{d^2 h(q)}{dq^2} |_{q=1}], \end{aligned} \quad (\text{B3})$$

where the expression in square brackets is in fact,

$$D^{rel}(q) \approx q \left[\frac{dh(q)}{dq} |_{q=1} + \frac{1}{2} (q - 1) \frac{d^2 h(q)}{dq^2} |_{q=1} \right]. \quad (\text{B4})$$

Expansion (in the vicinity of $q = 1$) in Eq. (B4) emphasizes that $D^{rel}(q)$ depends on the successive derivatives of the generalized Hurst exponent as parameters (calculated at $q = 1$).

For instance, combining Eqs. (6) with (10), we obtain an expression,

$$\begin{aligned} D^{rel}(q = 1) &= \frac{1}{\ln s} \sum_{\nu=1}^{N_d} p(\nu, s) \ln p(\nu, s) \\ &= \frac{1}{\ln s} \langle \ln p(\nu, s) \rangle = \frac{1}{\ln s} I_{q=1}(s), \end{aligned}$$

or equivalently

$$D(q = 1) = D(q = 0) + \frac{1}{\ln s} I_{q=1}(s), \quad (\text{B5})$$

here $\langle \dots \rangle = \sum_{\nu=1}^{N_d} p(\nu, s) \dots$ and $I_{q=1}(s)$ can be identified with the Shanon information (within the scale of s).

Finally, from Eqs. (B4) and (B5) we get,

$$\frac{1}{\ln s} I_{q=1}(s) = \frac{dh(q)}{dq} \Big|_{q=1} \quad (\text{B6})$$

for s from the scaling region. Thus, the change of the generalized Hurst exponent at $q = 1$ is the key to the Shanon information.

3. Case $q \rightarrow 2$

The correlation integral (or autocorrelation function) is obtained from the q -correlation function by substituting $q = 2$. Grassberger and Procaccia introduced both quantities long ago [68]. They proved that the statistical sum given by Eq. (6), transforms into a q -correlation function. From Eq. (9) we get (for large s for the scaling region) the reduced correlative dimension in the form,

$$D^{rel}(q = 2) \approx \frac{\ln Z_{q=2}(s)}{\ln s}$$

or equivalently

$$D(q = 2) \approx D(q = 0) + \frac{\ln Z_{q=2}(s)}{\ln s}. \quad (\text{B7})$$

4. General case of arbitrary q : Bounds

a. Properties of D

In our situation (see Eq. (14) and Fig. 5 for help) Rényi dimensions fulfill general inequalities/bounds which are not identical to those well known for the ordinary Rényi dimensions. The differences result from the fact that $D(q)$ is not in our case the monotonic function of q (see Fig. 5(e) for details), i.e., the Hentschel-Procaccia inequality [67] is valid in our case only on disjoint intervals q . These bounds are as follows,

- (i) $D(q) > 0$, for arbitrary value of q ;
- (ii) $(q' - 1)D(q') > (q - 1)D(q)$ for $q' > q$;
- (iii) if $D(q') < D(q)$ for $q' > q$ (i.e., if we deal with monotonically decreasing ranges of $D(q)$) then $\frac{q'-1}{q'}D(q') > \frac{q-1}{q}D(q)$, where $q', q \neq 0$, otherwise the opposite inequality is fulfilled.

From (iii) we obtain,

- (a) $D(q) < \frac{q}{q-1}D(q = +\infty)$ for $q > 1$;
- (b) $D(q) > \frac{q}{q-1}D(q = -\infty)$ for $q < 0$, where $D(q = -\infty)$ is finite.

b. Properties of f

We begin with general useful property of the $f(\alpha(q))$ spectrum. From Eqs. (14) and (17)

$$f(\alpha(q)) = D(q) + q(q - 1)D'(q), \quad (\text{B8})$$

where we marked $D'(q) = \frac{dD(q)}{dq}$. Note that the intermediate step in the derivation of the above formula is the following convenient expression obtained from Eq. (14) and the first equality in Eq. (17),

$$\alpha(q) = D(q) + (q - 1)D'(q). \quad (\text{B9})$$

Hence, for $q = 1$ and extreimums of $D(q)$ we have,

$$\alpha(q) = D(q). \quad (\text{B10})$$

However, you have to see that the location of the extremes of the functions $\alpha(q)$ and $D(q)$ is different (see Figs. 5(e) and 5(f) for details).

Moreover, two characteristic limitations that can significantly distinguish multi-branched multifractality from ordinary (i.e., single-branched) multifractality we present. Namely, from Eq. (B10) we get,

$$\begin{aligned} \alpha(q = +\infty) &= D(q = +\infty) \\ \alpha(q = -\infty) &= D(q = -\infty), \end{aligned} \quad (\text{B11})$$

at assumption that derivative $D'(q)$ disappears faster than $1/q$ if $|q| \rightarrow \infty$. It should be emphasized that because $\alpha(q)$ is not a monotonically decreasing function of q (see Fig. 5(f) for details), in general $\alpha(q = +\infty) \neq \alpha_{min}$ and $\alpha(q = -\infty) \neq \alpha_{max}$, where α_{min} and α_{max} are the minimal and maximal values of $\alpha(q)$, respectively.

From Eq. B8 the special cases yield,

$$\begin{aligned} f(\alpha(q = 0)) &= D(q = 0) = \alpha(q = 0) + D'(q) \Big|_{q=0}, \\ f(\alpha(q = 1)) &= D(q = 1) = \alpha(q = 1), \end{aligned} \quad (\text{B12})$$

where we get $\frac{df(\alpha(q))}{d\alpha} \Big|_{\alpha(q=1)} = 1$ (with help of Eq. (18)). This relation and the second equality in Eq. (B12) defines the contact point considered in Sec. II E.

[1] P. Oświęcimka, J. Kwapienie, and S. Drożdż, *Phys. Rev. E* **74**, 016103 (2006).

[2] J. Kwapienie and S. Drożdż, *Phys. Rep.* **515**, 115 (2012).

[3] P. Oświęcimka, S. Drożdż, M. Forczek, S. Jadach, and J. Kwapienie, *Phys. Rev. E* **89**, 023305 (2014).

[4] S. Drożdż, P. Oświęcimka, *Phys. Rev. E* **91**, 030902(R) (2015).

[5] B.B. Mandelbrot, *A Multifractal Walk Down Wall Street*, *Scientific American* **280**(2), 70 (1999).

[6] S. Drożdż, R. Gębarowski, L. Minati, P. Oświęcimka, and M. Wątorek, *Chaos* **28**, 071101 (2018).

[7] Cuangxi Cao, Ling-Yen He, Jie Cao: *Multifractal Detrended Analysis Method and Its Applications in Financial Markets* (Springer, 2018)

[8] C. Beck and F. Schlogl, *Thermodynamics of chaotic systems. An introduction* (Cambridge Univ. Press, Cambridge 1995).

[9] Z.-Q. Jiang, W.-J. Xiea, W.-X. Zhoua and D. Sornette, arXiv:1805.04750 (2018).

[10] J. Perelló, J. Masoliver, A. Kasprzak, and R. Kutner, *Phys. Rev. E* **78**, 036108 (2008).

[11] A. Kasprzak, R. Kutner, J. Perelló, J. Masoliver, *Eur. Phys. J. B* **76**, 513 (2010).

[12] B.B. Mandelbrot, C.J.G. Evertsz, and Y. Hayakawa, *Phys. Rev. A* **42**, 4528 (1990).

[13] B.B. Mandelbrot and C.J.G. Evertsz *Exactly Self-similar Left-sided Multifractals in Fractals and Disordered Systems* A. Bunde and S. Havlin (Eds.) (Springer-Verlag, Haidelberg, New York 1996), Chapt. 10.

[14] R. Blumenfeld and A. Aharony, *Phys. Rev. Lett.* **62**, 2977 (1989).

[15] T. Bohr, P. Cvitanović, and M. H. Jensen, *Europhys. Lett.* **6**, 445 (1988).

[16] J. Lee and H.E. Stanley, *Phys. Rev. Lett.* **61**, 2945 (1988).

[17] M.H. Jensen, G. Paladin, and A. Vulpiani, *Phys. Rev. E* **50**(6), 4352 (1994).

[18] Th.C. Halsey, K. Honda, and B. Duplantier, *J. Stat. Phys.* **85**, 681 (1996).

[19] D. Schertzer, S. Lovejoy and P. Hubert, *An Introduction to Stochastic Multifractal Fields*, ISFMA Symposium on Environmental Science and Engineering with related Mathematical Problems, Beijing, A. Ern and W. Liu (Eds.), *High Education Press* **4**, 106 (2002).

[20] B. Enescu, K. Ito and Z.R. Struzik, *Geophysical Journal International*, **164**, 63-74 (2006).

[21] M. V. Rodkin, *Izvestiya Physics Sol. Earth.* **37**, 663 (2001).

[22] D. Sornette and G. Ouillon, *Phys. Rev. Lett.* **94**, 038501 (2005).

[23] S. Lovejoy and D. Schertzer, *The Weather and Climate. Emergent Laws and Multifractal Cascades* (Cambridge Univ. Press, Cambridge 2013).

[24] Xu Jing-Jing and Hu Fei, *Atmospheric and Oceanic Science Lett.* **8**, 72 (2015).

[25] B. B. Mandelbrot, *Fractals and Scaling in Finance* (Springer-Verlag, New York, 1997).

[26] Yasmine Hayek Kobeissi, *Multifractal Financial Markets. An Alternative Approach to Asset and Risk Management*, Springer Briefs in Finance (Book 4) (Springer-Verlag, Berlin 2013).

[27] A. L. Karperien, H. Jelinek, N. Milosevic, *Multifractals: a review with an application in neuroscience* in Proceed. of 18th INTERNATIONAL CONFERENCE ON CONTROL SYSTEMS AND COMPUTER SCIENCE: APPLICATIONS OF FRACTAL ANALYSIS IN MEDICINE IAFA 1.5 Multifractals: a Review with an Application in Neuroscience, May 2011, p. 1.

[28] D. Fettendorf, R. A. Kraft, R. A. Sandler, I. Opris, Ch. A. Sexton, V. Z. Mamarellis, R. E. Hampson, S. A. Deadwyler, *Front. Syst. Neurosci.* **9**, 130 (2015).

[29] en.wikipedia.org/wiki/Cardiophysics

[30] J. T. Flick and J. Joseph, *Method for Diagnosing Heart Disease, Predicting Sudden Death and Analyzing Treatment Response Using Multifractal Analysis*, United States Patent US6993377 B2, 31 January 2006.

[31] P.Ch. Ivanov, L.A. Nunes Amaral, A.L. Goldberger, S. Havlin, M.G. Rosenblum, H.E. Stanley and Z.R. Struzik, *CHAOS, An Interdisciplinary Journal of Nonlinear Science* **11**, 641-652 (2001).

[32] Z.R. Struzik, J. Hayano, R. Soma, S. Kwak and Y. Yamamoto, *IEEE Transactions on Biomedical Engineering* **53**, 89-94 (2006).

[33] Z. Nagy, P. Mukli, P. Herman, and A. Eke, *Frontiers in Physiology. Methods Article*, **26** July 2017, doi.org/10.3389/fphys.2017.00533.

[34] D. Grech and G. Pamua, *Acta Phys. Pol. A* **121**, B-34 (2012).

[35] L. Czarnecki and D. Grech, *Acta Phys. Pol. A* **117**, 623 (2010).

[36] J. Ludescher, M. I. Bogachev, J. W. Kantelhardt, A. Y. Schumann, A. Bunde, *Physica A* **390**, 2480 (2011).

[37] A. Y. Schumann and J.W. Kantelhardt, *Physics A* **390**, 2637 (2011).

[38] J. W. Kantelhardt, S. A. Zschiegner, E. Koscielny-Bunde, A. Bunde, S. Havlin, and H. E. Stanley, *Physica A* **316**, 87 (2002).

[39] J.-P. Bouchaud, M. Potters, and M. Meyer, *Eur. Phys. J. B* **13**, 595 (2000).

[40] M. Montero and J. Masoliver, *Phys. Rev. E* **76**, 061115 (2007).

[41] V. Tejedor and R. Metzler, *J. Phys. A: Math. Theor.* **43**, 082002 (2010).

[42] M. Magdziarz, R. Metzler, W. Szczotka, and P. Żebrowski, *J. Stat. Mech.*, P04010 (2012).

[43] P. Oświęcimka, J. Kwapienie, S. Drożdż, *Physica A* **347**, 626 (2005).

- [44] P. Oświęcimka, J. Kwapienie, R. Rak, *Acta Phys. Pol. B* **36**, 2447 (2005).
- [45] P. Oświęcimka, S. Drożdż, R. Gębarowski, A.Z. Górska, J. Kwapienie, *Acta Phys. Pol. B* **46** 1579 (2015).
- [46] M. Denys, T. Gubiec, R. Kutner, M. Jagielski and H.E. Stanley, *Phys. Rev. E* **94**, 042305 (2016).
- [47] J. W. Haus and K. W. Kehr, *Phys. Rep.* **150**, 263 (1987).
- [48] J.-P. Bouchaud and A. Georges, *Phys. Rep.* **195**, 127 (1990).
- [49] J. Klamut, T. Gubiec, arXiv:1807.01934 [q-fin.ST] (2018).
- [50] W. Feller, *An Introduction to Probability Theory*, Vols. 1 and 2, Wiley, New York (1971).
- [51] E. Scalas, *Physica A* **362**, 225 (2006).
- [52] E. Scalas, *Chaos Soliton. Fract.* **34**, 33 (2007).
- [53] M. Politi and E. Scalas, *Physica A* **387**, 2025 (2008).
- [54] www.opentradingsystem.com/quantNotes/
- [55] D. Grech and Z. Mazur, *Acta Phys. Pol. B* **36**, 2403 (2005).
- [56] T. Gubiec and M. Wiliński, *Physica A* **432**, 216 (2015).
- [57] R. Rak and D. Grech, *Physica A* **508**, 48 (2018).
- [58] J. Klamut and T. Gubiec, *Eur. Phys. J. B*, 1 (2019).
- [59] P. Jizba and Jan Korbel, *Modeling Financial Time series: Multifractal Cascades and Rényi Entropy*, Interdisciplinary Symposium on Complex Systems, Emergence, Complexity and Computation 8 (ISCS) 2013, A. Sanayes, I. Zelinka, and O.E. Rssler (Eds.) (Springer-Verlag, Berlin, Heidelber 2014), p. 227.
- [60] Q. Cheng, *Nonlin. Processes Geophys.*, **21**, 477 (2014).
- [61] P. Jizba and T. Arimitsu, *Annals of Physics* **312**, 17 (2004).
- [62] M. Kale and F. B. Butar, *J. Math. Sci & Math. Edu.* **5**, 5 (2011).
- [63] B. B. Mandelbrot, Benoit B, *Physica Scripta* **32**, 257 (1985).
- [64] T. Gneiting and M. Schlather, *SIAM Review* **46**, 269 (2004).
- [65] A. F. Boriviera, *Physica A* **390**, 4426 (2011).
- [66] G. Jaeger, *Arch. Hist. Exact Sci.* **53**, 51 (1998).
- [67] H.G.E. Hentschel and I. Procaccia, *Physica D Non-linear Phenomena* **8**(3), 435 (1983).
- [68] P. Grassberger and I. Procaccia, *Phys. Rev. Lett.* **50**, 346 (1983).